

Nanostructured ferrite/graphene/polyaniline using for supercapacitor to enhance the capacitive behavior

M.A. Mousa¹ · M. Khairy^{1,2} · M. Shehab¹

Received: 25 August 2016 / Revised: 8 October 2016 / Accepted: 22 October 2016 / Published online: 4 November 2016
© Springer-Verlag Berlin Heidelberg 2016

Abstract Graphene nanosheets, polyaniline (PANI), and nanocrystallites of transition metal ferrite { Fe_3O_4 (Mag), NiFe_2O_4 (NiF), and CoFe_2O_4 (CoF)} have been prepared and characterized via XRD, FTIR, SEM, TEM, UV–vis spectroscopy, cyclic voltammetry, galvanostatic charge discharges, and impedance spectroscopy. Electrochemical measurements showed that supercapacitances of hybrid electrodes made of the ternary materials are higher than that of hybrid electrode made of binary or single material. The ternary hybrid CoF/graphene (G)/PANI electrode exhibits a highest specific capacitance reaching 1123 Fg^{-1} , an energy density of 240 Wh kg^{-1} at 1 A g^{-1} , and a power density of 2680 Wkg^{-1} at 1 A g^{-1} and outstanding cycling performance, with 98.2% capacitance retained over 2000 cycles. The extraordinary electrochemical performance of the ternary CoF/G/PANI hybrid can be attributed to the synergistic effects of the individual components. The PANI conducting polymer enhances an electron transport. The Ferrite nanoparticles prevent the restocking of the carbon sheets and provide Faradaic processes to increase the total capacitance.

Keywords Graphene · Supercapacitor · Ferrite · Cyclic voltammetry

Electronic supplementary material The online version of this article (doi:10.1007/s10008-016-3446-6) contains supplementary material, which is available to authorized users.

✉ M. Khairy
moh_khairy3@yahoo.com

¹ Chemistry Department, Faculty of Science, Benha University, Benha, Egypt

² Chemistry Department, College of Science, Al Imam Muhammad Ibn Saud Islamic University, Riyadh, Kingdom of Saudi Arabia

Introduction

With the rapidly developing market in portable electronic devices, electric vehicles, and hybrid electric vehicles, there has been a regularly expanding interest in environmentally friendly, high-performance energy storage systems. The recent research efforts on electrochemical power sources, such as batteries, electrochemical capacitors, and fuel cells, are coordinated toward accomplishing high specific energy, high specific power, long cycle life, etc., at a moderately low cost [1].

Since batteries have a good energy density at the cost of a lesser power density, a supercapacitor could be introduced with a specific end goal to supplement the batteries. A supercapacitor has a good power density, but a lower energy density. This ability makes it suitable to give energy during short power peaks. The long lifetime of the supercapacitor likewise makes it suitable to use to smooth out the power to the battery and thereby relieve the battery from stress. The electrochemical supercapacitors are considered as a piece of a vast area of electrochemical energy storage in light of the fact that they span over any barrier between other capacitors and batteries [2]. The fundamental purposes of the supercapacitors are identified with high power density, large peak power requirements, load smoothing, reinforcement power for mobile applications, and diverse types of recovering systems. Supercapacitors can be easily and quickly charged from different electrical supply sources, and also, their voltage–current characteristics and charging/discharging behaviors are not affected by the over-current, deep discharge, and temperature variations. Supercapacitors have the capacity for backing up to millions of life cycles [3].

Capacitance must be seen subjectively with the help of the model for a porous electrode and as a quantity strongly depending on electrical potential [4]. Despite the fact that carbon materials (such as carbon nanotubes (CNTs) (have a much higher electronic conductivity) /active carbon) and polyaniline

(PANI) are widely studied as electrode materials, the utilization of these individual materials in supercapacitors is restricted because of their disadvantages, for example, the high cost of CNTs, the unsuitable performance of active carbon, and poor life of PANI. At the point when the benefits of carbon materials are consolidated with PANI, the subsequent composites give synergistic execution as electrode materials [5].

Graphene and chemically modified graphene sheets have high conductivity [6], high surface area, and good mechanical properties similar to or far and away superior to carbon nanotubes. Simple chemical treatment of graphite can be used easily to synthesize the graphene-based materials. Therefore, the capability of utilizing graphene-based materials for supercapacitor has attracted very much attention very recently [7]. In fact, specific capacitances of tens to 135 Fg^{-1} have been resolved for distinctive graphene materials [8].

Transition metal oxides linked to carbon nanotubes have been studied and show enhanced capacitive behavior because of their enhanced stability and high conductivity [9]. In this way, the hybrid of an electric double-layer system and a Faradaic pseudocapacitive system could be a good candidate for a supercapacitor with high energy density and specific capacitance [10–13].

The appearance of new organic and inorganic nanomaterials in later years, especially, graphene, conducting polymers, and metal oxides, has enabled the formation of high-performance energy devices. Therefore, in the present paper, we studied the electrochemical behavior of nanoferrites (Fe_3O_4 , NiFe_2O_4 , or CoFe_2O_4), polyaniline, and binary as well as a ternary system of them as advanced capacitor materials. This ternary material is predictable to revoke the drawbacks of each component, which produce a high specific capacitance and an excellent cycling life.

Experimental

Preparation of graphene nanosheets

To a mixture of fuming nitric acid (25 ml) and sulfuric acid (50 ml) for 30 min, 5.0 g of graphite (99.99% purity, provided from Fischer Scientific, Chemical) was gradually added. After cooling the mixture down to 5°C in an ice bath, 25.0 g of potassium chlorate was gradually added to the solution while stirring for 30 min. The solution was heated up to 70°C for 5 h and was then put on the air for 3 days. Most graphite precipitated at the bottom, but some reacted carbons were floating. The floating carbon materials were transferred into deionized water (1 L). The solution was directly filtrated after stirring it

for 1 h, and then, the sample was dried in air. Afterward, the previous steps were repeated four times.

The previously mentioned method for preparing graphene is similar to the Staudenmaier process [14, 15] utilized for developing graphite oxide. On the other hand, unlike the Staudenmaier process which filtrates all the graphite powders, we separate out (by filtering) just the floating graphite, which has reacted with the potassium chlorate.

Preparation of conducting polymer polyaniline

Into 100 ml nitric acid (1 M), 1.82 ml aniline (supplied from Merck) was added and stirred. In a drop-wise fashion, 5.7 g $(\text{NH}_4)_2\text{S}_2\text{O}_8$ in 100 ml deionized water was then added into the previous solution as an oxidant and stirred for 2 h at room temperature. After filtration, deionized water, methanol, and acetone were used to wash the precipitate until the filtrate was colorless. The dark green polyaniline powder was dried at 60°C .

Preparation of magnetite (Fe_3O_4 (Mag))

Magnetite (Fe_3O_4) was prepared from ferrous chloride and ferric chloride by a modified method as described elsewhere [16]. Solution A, 3.2 g of ferric chloride in 15 ml concentrated HCl, and solution B, 2 g of ferrous chloride in 20 ml concentrated HCl and ammonia solution 33% as an alkali source, were prepared as stock solutions. The solution A was mixed with solution B under vigorous and continuous stirring. Thirty-milliliter ammonia solution was added to the mixture slowly. A black precipitate of iron oxides was formed immediately and filtrated and then washed several times with deionized water.

Preparation of CoFe_2O_4

The stoichiometric amounts of cobalt nitrate $\text{Co}(\text{NO}_3)_2 \cdot 6\text{H}_2\text{O}$ (6.20 g) and ferric nitrate $(\text{Fe}(\text{NO}_3)_3 \cdot 9\text{H}_2\text{O})$ (17.22 g) were dissolved in deionized water under magnetic stirring. Then, citric acid ($\text{C}_6\text{H}_8\text{O}_7 \cdot \text{H}_2\text{O}$) (13.43 g) was mixed with the metal nitrate solution to chelate Co^{2+} and Fe^{3+} ions in the solution. The molar ratio of citric acid to total moles of nitrates that were used is 1:3. A definite amount of ammonia solution was added dropwise to the solution to adjust the pH value at 7 and stabilize the citrate–nitrate solution. The neutralite solution was evaporated to dryness by heating at 90°C on a hot plate with continuous stirring until it becomes viscous and finally formed a very viscous gel. The gel was dried by raising the temperature up to 120°C . The dried gel burnt completely in a self-propagating combustion manner to form a loose powder. Finally, the as-burnt powders were annealed at temperature 800°C for 4 h to obtain the spinel CoFe_2O_4 phase.

Preparation of NiFe₂O₄

The same preparation method mentioned for cobalt ferrite preparation was used to prepare NiFe₂O₄ using Ni(NO₃)₂·6H₂O instead of Co(NO₃)₂·6H₂O.

Characterization tools

X-ray diffraction

XRD analyses were performed on a Philips X-ray diffractometer. The patterns were run with filtered Co-*K*_α radiation ($\lambda = 1.79 \text{ \AA}$). The diffractogram was recorded for 2θ angles in the range 15–80°.

Scanning and transmission electron microscope

The SEM photographs were taken with a scanning electron microscope (Philips SEM 515), and a JEM-2100f (JEOL, Japan) was used to perform the TEM analyses of the samples.

Fourier transform infrared spectroscopy spectroscopy

An infrared spectrophotometer (PerkinElmer LX 18–5255) was used to record the FTIR spectra in the range of 400–4000 cm⁻¹. The samples were grounded with KBr (1:100) so as to form tablets, which mounted into the sample holder in the cavity of the spectrometer.

UV–visible spectra

UV–visible absorption spectra were measured using a Shimadzu UV-2501PC spectrophotometer in the range of 300–800 nm.

Electrochemical performance measurements

The electrodes for capacitance measurement were fabricated by forming a paste of the graphene, polyaniline, or ferrite samples with a binder polytetrafluoroethylene (1%, w/w) with the mass ratio 95:5 to obtain a homogeneous slurry. The paste was spread using a doctor blade and roll-pressed uniformly onto an indium tin oxide (ITO) glass (Pilkington Kappa Energy Float), transmission ca. 80% in the visible and sheet resistance 18–20 $\Omega \text{ cm}$, that serves as current collector. It is then dried at 100 °C to make sure that the entire solvent is evaporated. The binary and ternary multilayer films were prepared using a layer-by-layer deposition of positively charged ferrite NPs and negatively charged graphene (G) suspension

onto the precleaned ITO glass. For a typical layer-by-layer assembly based on spin coating, one drop of the ferrite solution (1 mg ml⁻¹, pH 4) was dropped on cleaning the substrate and spinning at 400 rpm for 20 s. Then, drying of the substrate was carried out. Furthermore, the graphene solution (2 mg ml⁻¹, pH 3.5) was dropped on the substrate coated with ferrite layer, spinning for 20 s at 400 rpm, and dried through the same way. Then, a drop of polyaniline solution (1 mg ml⁻¹, acetone) dropped on the substrate coated with ferrite layer and graphene layer, spinning for 20 s at 400 rpm, and then dried. The electrode assembly is shown in Fig. S1.

The electrochemical properties of the electrodes were studied using a three-electrode cell consisted of a standard calomel electrode (SCE), a Pt mesh as the counter electrode, and a working electrode. The electrolyte used in all measurements was an aqueous solution of 6 M KOH. Cyclic voltammetry (CV), constant current charge–discharge tests, and electrochemical impedance spectroscopy (EIS) experiments were conducted using a Gamry G750 potentiostat/galvanostat instrument carried out with the EIS300 software.

Results and discussions

X-ray powder diffraction

The XRD diffraction patterns of pure ferrites, PANI, and graphene are shown in Fig. 1a–e. Figure 1a–c shows the typical reflections of (220), (311), (222), (400), (422), (511), and (440) planes that are indications of the presence of the cubic spinel structure for Fe₃O₄ (JCPDS 19-629), NiFe₂O₄ (JCPDS 074-2081), and CoFe₂O₄ (JCPDS 22-1086). The sharp peaks represent that all ferrites are crystalline nature of single phase. The peaks at the 2θ values of 18.3, 30.1, 35.3, 37.1, 43.0, 53.5, 56.9, and 62.43° can be indexed as the (111), (220), (311), (222), (400), (422), (511), and (440) crystal planes of spinel, respectively. Figure 1d shows the XRD pattern of PANI. The partly crystalline structure of PANI was observed from the XRD pattern due to the appearance of a broad peak at 2θ of ~20°. This is because the phenyl rings were densely packed and, thus, an extensive π – π orbital overlap [17]. The XRD patterns of graphene (Fig. 1e) show one broad reflection peak centered at $2\theta = 25.3^\circ$ (002), which is attributed to an interlayer spacing of 0.38 nm. The broad peak observed is an evidence to that the graphene sheets are loosely stacked and it is distinct than that of the crystalline graphite. The absence of any peak characterized for graphene oxide or graphite indicates that the prepared sample is pure graphene [6].

The crystallite sizes of the ferrites and PANI were estimated from the X-ray peak broadening of the (311) peak for ferrites

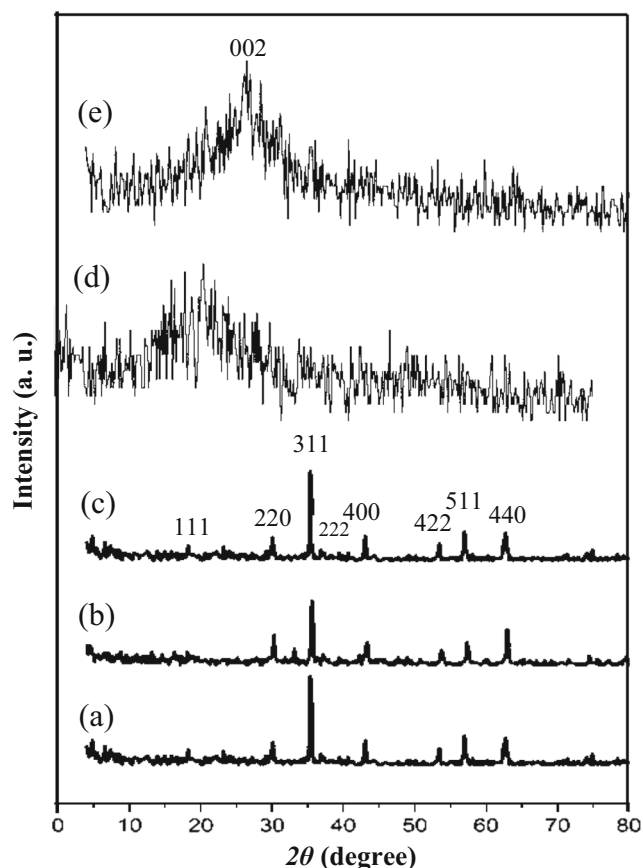


Fig. 1 XRD pattern of **a** CoF, **b** NiF, **c** Mag, **d** PANI, and **e** G

and (002) peak for PANI using Scherrer's equation [18] and found to be 40.7, 43.8, and 50.0, 21.0 nm for NiFe_2O_4 , CoFe_2O_4 , Fe_3O_4 , and PANI, respectively.

Transmission electron microscopy and scanning electron microscopy study

Figure 2 shows the TEM images of the prepared samples as well as the selected area electron diffraction (SAED). The TEM images (Fig. 2a) of graphene show nanosheets rippled and entangled with each other. They are transparent and reveal stable nature under the electron beam; they are acting as monolayer graphene nanosheets. The SAED on a region along the [001] zone axis shows that the well-defined diffraction spots prove the crystalline structure of the graphene nanoplatelets obtained. The TEM image of polyaniline, shown in Fig. 2b, illustrates that the prepared sample is composed almost entirely of nanofibers having an average fiber diameter in the range 15–20 nm.

The TEM images of magnetite given in Fig. 2c show that the morphological structure of Fe_3O_4 (Mag) consists of nanowires with an average diameter of 50 nm. The SAED ring

patterns (seen in Fig. 2c) were consistent with those of magnetite. The TEM images of the synthesized CoFe_2O_4 and NiFe_2O_4 , (seen in Fig. 2d, e) show that the particles are mostly in the form of squares, parallelells, and truncated forms. Moreover, some moderately agglomerated particles, as well as separated particles, were also observed. The appearance of a large number of small scattered grains with the strongest spotty patterns as observed in TEM images indicating highly crystalline spinel structure with a range of particle size lies in 20–50 nm. The SAED pattern of investigated samples shows their high crystallinity structure.

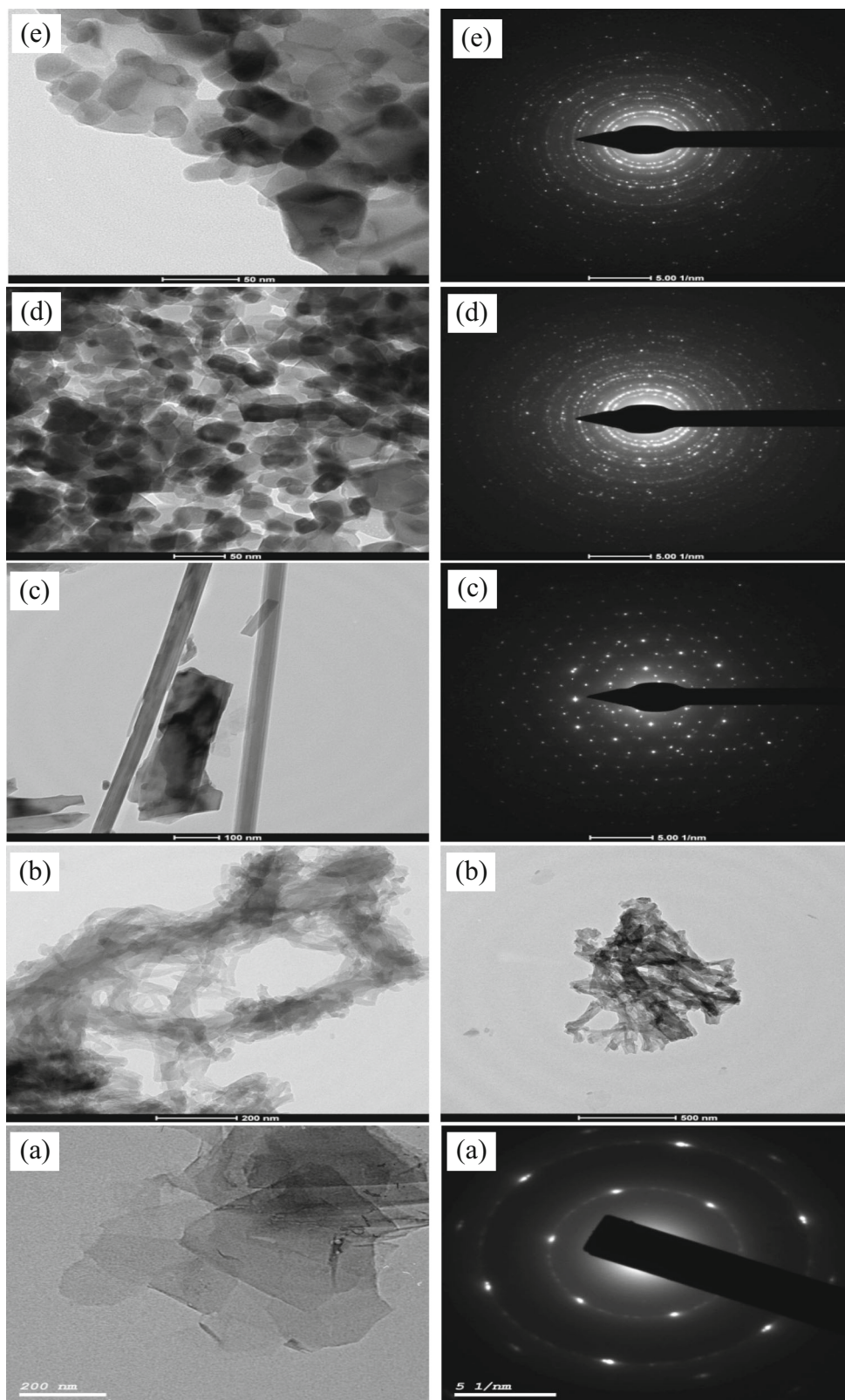
Scanning electron micrographs of all the prepared samples are shown in Fig. 3. It can be seen that the surface morphology differs from sample to another, and it also agrees well with the results obtained from TEM micrographs.

Fourier transform infrared spectroscopy results

FTIR spectra of all studied samples are measured in the range of 400–4000 and shown in Fig. 4. The FTIR spectrum of the graphene nanosheets shows a prominent peak in the region 1626–1690 cm^{-1} with a center at $\sim 1650 \text{ cm}^{-1}$, which could be assigned to the ring vibration of the whole carbon skeleton of graphene [19] indicating the successful synthesis of graphene sheets.

The FTIR spectrum of PANI sample (Fig. 4b) shows the main characteristic bands of polyaniline, which are assigned as follows: the bands located at 1583 and 1497 cm^{-1} are attributed to the characteristic C–N stretching vibration of the quinoid N=Q=N and benzenoid N–B–N rings [20], respectively (where B refers to the benzoic-type rings and Q refers to the quinonic-type rings). These peaks indicate the oxidation state of the emeraldine salt of PANI. The peak that appeared at 1138 cm^{-1} of PANI can be attributed to the doped PANI chain with H^+ and was commonly observed in the spectrum of emeraldine base (EB) protonated with strong acids [17]. The characteristic peaks at 1138 and 826 cm^{-1} were assigned to B–NH–Q or B–NH–B bonds and out-of-plane bending vibration of the C–H on the P-disubstituted aromatic ring, respectively. The peak that appeared at 1138 cm^{-1} , which is the characteristic of PANI conductivity and the degree of the delocalization of electrons, was attributed to the in-plane bending vibration of the C–H [20]. The band at 1383 cm^{-1} in this spectrum is assigned to the stretching of C–N bonds of secondary aromatic amines and/or displacement of π electrons that is induced by acid doping of the polymer [21]. The band characteristic of the electrically conductive form of doped polyaniline is observed at ca. 1305 cm^{-1} . This was attributed to when the EB polyaniline doped with acid, the C–N⁺ polaron structure was produced [22].

Fig. 2 TEM micrographs and SAED pattern of **a** G, **b** PANI, **c** Mag, **d** CoF, and **e** NiF



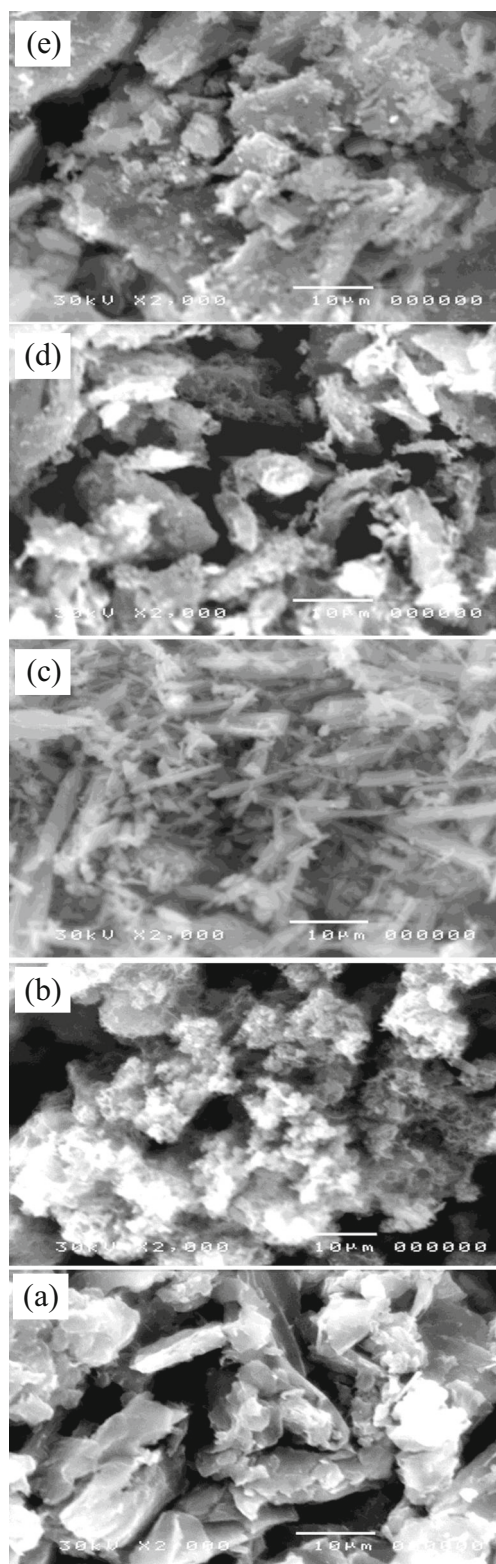


Fig. 3 SEM micrographs of the prepared samples: **a** G, **b** PANI, **c** Mag, **d** CoF, and **e** NiF

The FTIR spectra of the ferrite samples showed the characteristic tetrahedral vibration bands ν_1 (600–450 cm^{-1}) and the octahedral vibration band ν_2 (420–

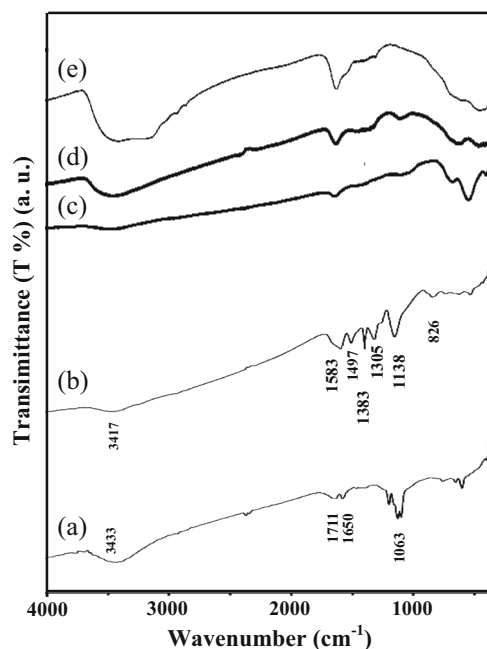


Fig. 4 FTIR spectra of **a** graphene, **b** PANI, **c** Mag, **d** NiF, and **e** CoF

350 cm^{-1}) of ferrite spinel samples (Fig. 4c–e) [23]. The stretching and bending mode vibrations of the free or absorbed water were confirmed by appearing prominent bands near 3400 and 1600 cm^{-1} [24].

UV–vis absorption spectra

UV–vis absorption spectrum for as-synthesized graphene nanosheets was also investigated (Fig. S2). A sharp absorbance peak centered at around 261 nm has been observed. The absorbance peak is well aligned with the absorption spectrum reported in the literature [2, 3, 25] and generally assigned to the excitation of π -plasmon of the graphitic structure.

Electrochemical measurements

The cyclic voltammogram (CV) tests were carried out within a potential range of -0.8 to 0.2 V with scan rates varying from 1 to 20 mV s^{-1} using 6 M KOH electrolyte. Figure 5 illustrates the CV curves of the single-material electrodes: graphene, polyaniline, Fe_3O_4 , NiFe_2O_4 , and CoFe_2O_4 recorded at a scan rate of 1 mV s^{-1} . The CV profile of graphene clearly indicates the capacitive behavior with a semirectangular shape without any peaks, which is a characteristic of the electric double-layer capacitance of carbon-based materials. On the other hand, polyaniline and ferrite electrodes demonstrate a couple of redox peaks. The redox peaks of PANI are attributed to two processes: the first is the redox transition between a semiconducting state (leucoemeraldine form) [26] and a conducting state (polaronic emeraldine form), and the second is the Faradic transformation of emeraldine/pernigraniline [8]. The

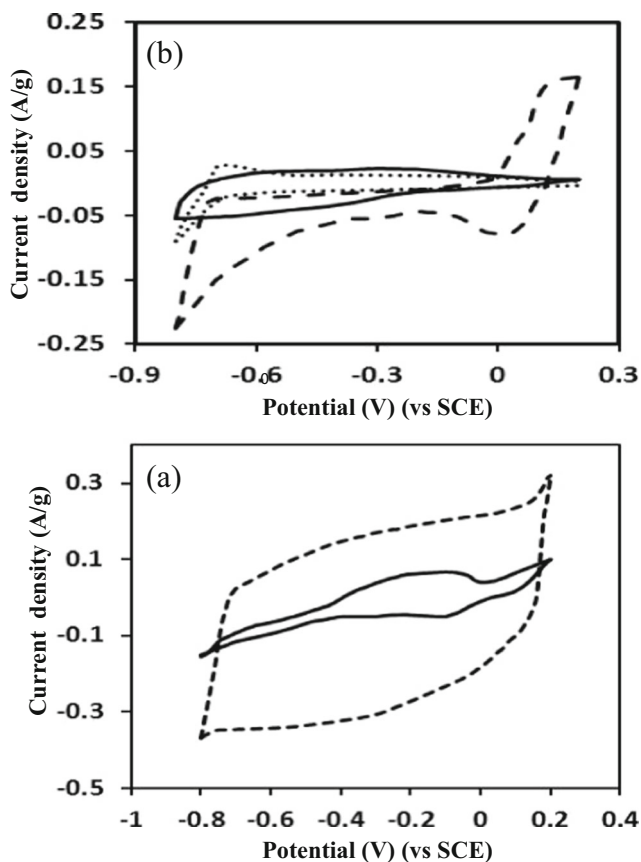


Fig. 5 Cyclic voltammograms (CV) in 6 M KOH at a sweep rate of 1 mV s⁻¹: **a** G (dashed line) and PANI (continuous line). **b** Mag (dotted line), NiF (continuous line), and CoF (dashed line)

specific capacitances (C_{sp}) for all the investigated electrodes were computed from CV curves according to Eq. (1) [4, 27], and the results are listed in Table 1.

$$C_{sp} = \frac{1}{vw(\Delta V)} \int_{V_a}^{V_c} iVdV \tag{1}$$

where ΔV (V) is the potential drop, the scan rate is v (mV s⁻¹), and w (g) is the mass of the electrode. Graphene electrode exhibits the highest specific capacitance and showed a fast charge storage and transport kinetics (i.e., high-rate capability), which can be demonstrated by its rectangle shape and sharp fleeting responses at both ends of the CV plot (Fig. 5a). The mesoporosity, outstanding electrical conductivity, and electrolyte approachability of graphene could be responsible for the observed high-rate capability [28].

Figure 6 shows the CV loops of binary and ternary hybrid materials: G/PANI, G/NiFe₂O₄ (NiF), G/CoFe₂O₄ (CoF), G/Mag and PANI/CoF, PANI/Mag, PANI/NiF, graphene/CoFe₂O₄/polyaniline (G/CoF/PANI), G/NiF/PANI, and G/Mag/PANI recorded at a scan rate of 1 mV s⁻¹. The specific capacitance values C_{sp} for all electrode systems are also calculated by Eq. (1) and given in Table 1. From which, it can be seen that the specific capacitance (C_{sp}) increases as follows: ternary materials > binary materials > single material. The performance in capacitance of ternary materials may be attributed to the following reasons: first, the presence of ionic layer of polyaniline at the surface of electrode leads to enhancement of the electrolyte availability and kinetics of ion transport by effectively increasing the number of ion diffusion paths inside the bulk of electrode and also reduces the interfacial resistance between the electrolyte and the active electrode materials, therefore improving the performance. Second, the noticeable amount of pleats present in

Table 1 Capacitance data from CV curves and discharge data for the investigated samples

Electrode	C (Fg ⁻¹) from CV curves at 1 mV s ⁻¹	C (Fg ⁻¹) from discharge data at 1 A g ⁻¹
G	223	212
PANI	36	28
CoF	54	39
NiF	30	22
Mag	13	12
G/PANI	612	431
G/CoF	256	196
G/NiF	81	70
G/Mag	23	15
PANI/Mag	14.5	15.5
PANI/CoF	60	53
PANI/NiF	51	46
G/Mag/PANI	325	259
G/CoF/PANI	1123	805
G/NiF/PANI	645	462

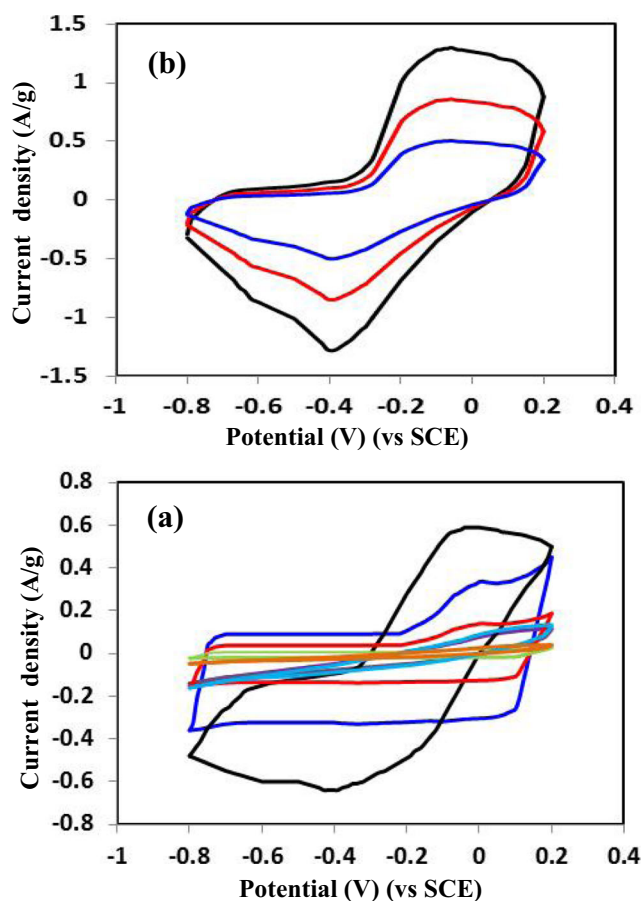


Fig. 6 CV curves in 6 M KOH at 1 mV s^{-1} of **a**) G/PANI (black line), G/CoF (royal blue line), G/NiF (red line), PANI/CoF (green line), PANI/Mag (orange line), PANI/NiF (light blue line). **b**) G/CoF/PANI (black line), G/NiF/PANI (red line), and G/Mag/PANI (royal blue line)

the graphene surface increases the quantity of mesopores that can be available to the ions of electrolyte. Additionally, a highly conductive network supplied from graphene causes an enhancement in the electron transport during the charge and discharge processes, subsequently increasing the electrical properties and charge transfer pathways generated of pure ferrite and polyaniline [29, 30].

As depicted in Table 1, the ternary G/CoF/PANI electrode shows a higher specific capacitance than all the other electrodes investigated. Thus, in order to get more information on the electrochemical behavior of this electrode, CV characterizations were done at different scan rates from 1 to 20 mV s^{-1} (Fig. 7). From which, it can be seen that the specific capacitance increases with increasing the scan rate, referring to the good rate property and excellent capacitance behavior. The non-rectangular nature of the CV curves and presence of peaks at high scan rate indicate deviation from ideal behavior and the considerable contribution of pseudocapacitance to the total specific capacitance. This behavior can be attributed to that K^+ may not have enough time to enter the deep body of

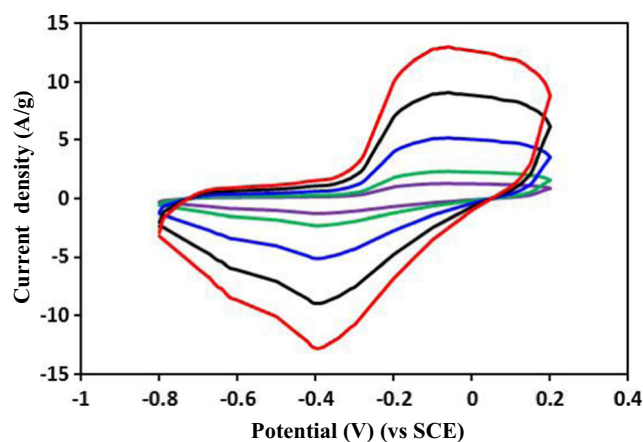


Fig. 7 CV curves of G/CoF/PANI in 6 M KOH at different scan rates: 20 mV s^{-1} (red line), 10 mV s^{-1} (black line), 5 mV s^{-1} (royal blue line), 2 mV s^{-1} (green line), and 1 mV s^{-1} (violet line)

the material and produced an accumulation of charge at the interface [31].

The electrochemical performances of the electrode materials were also investigated by galvanostatic charge/discharge measurements. The results obtained are represented in Fig. 8. All discharge curves showed an internal resistance drop (IR_{drop}). It was recognized to the equivalent series resistance that comprises both electrode and electrolyte resistances, in addition to the contact resistance among the electrodes, separator, and the electrolyte [31]. As opposed to graphene, the discharge curves of the double and ternary electrodes demonstrate a deviation from a straight line due to their pseudocapacitive nature. The longest discharge times observed for the ternary system indicate that it has the highest specific capacitance than the other systems. The specific capacitance of the electrodes was evaluated from the discharge cycles according to Eq. (2):

$$C_{\text{sp}} = I / \left[m \left(\frac{dV}{dt} \right) \right] \quad (2)$$

where I is the current loading (A), m is the mass of the active materials (g), and dV/dt is the discharge curve slope [1, 32]. The slope of a full discharge curve (aside from internal resistance (IR_{drop})) was taken to quantify the specific capacitance of the electrode. The results obtained are listed in Table 1. From which, it can be seen that G/CoF/PANI electrode exhibits the high capacity value. These feedbacks assist the specific capacitances obtained from the CV curves earlier.

It should be mentioned here that with introducing the graphene into electrode materials, a drop in the internal resistance (IR) was observed, indicating the decreasing resistance of the electrode. This is attributed to that the conductive graphene sheet could serve as a fast electron transport path in the electrode. The electroactive PANI/ferrite composite would favor high-density electron produced through fast and

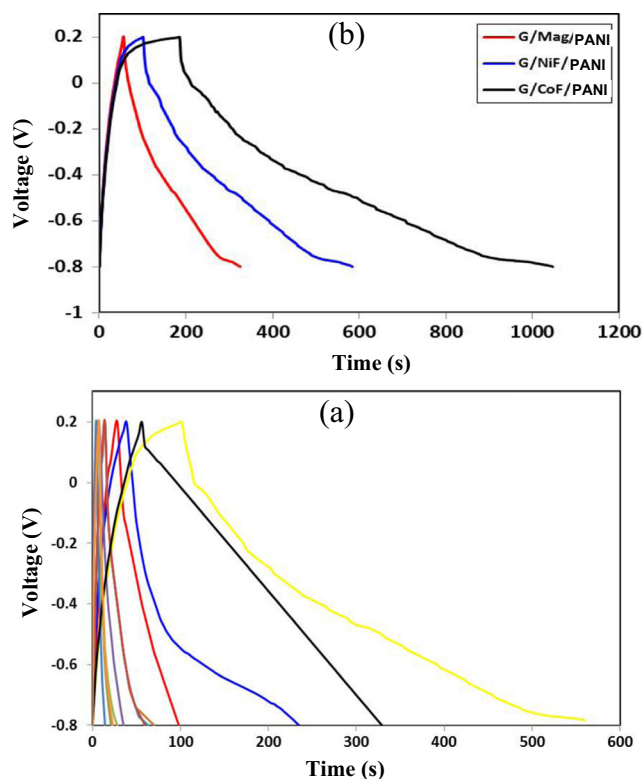


Fig. 8 Galvanostatic charge/discharge curves at 1 A g^{-1} for **a** G (black line), PANI (violet line), NiF (light green line), CoF (dark brown line), Mag (light blue line), G/CoF (royal blue line), G/NiF (red line), G/Mag (green line), G/PANI (yellow line), PANI/CoF (dark blue line), PANI/NiF (orange line), and PANI/Mag (light brown line). **b** G/Mag/PANI (red line), G/NiF/PANI (royal blue line), and G/CoF/PANI (black line)

reversible redox reaction. Consequently, the G/CoF/PANI electrode could obtain high electrochemical capacitance performance.

Rate capability is an important factor for using the supercapacitor in power application. A good electrochemical energy storage device is required to provide high energy density at a high charge/discharge rate. In the present work, the specific capacitances of the binary and ternary electrode materials at different galvanostatic current densities were studied and typical plots for the electrodes with higher capacitance values are shown in Figs. S3 and S4. For all the electrode materials, the capacities were found to decrease with increasing current rate discharge. This is due to the limited diffusion of K^+ with the time restriction at high scan rates. Only the outer active surface can be used for charge storing, resulting in a lower electrochemical utilization of electroactive materials [33, 34].

Long cycling stability is of great importance for supercapacitor operations. Therefore, the electrochemical stability of the ternary G/CoF/PANI electrode (highest C_{sp}) was studied, at a current density of 1 A g^{-1} . The results obtained are represented in Fig. 9. As seen in the figure after 2000 cycles, the G/CoF/PANI electrode retained about 98.2% of its

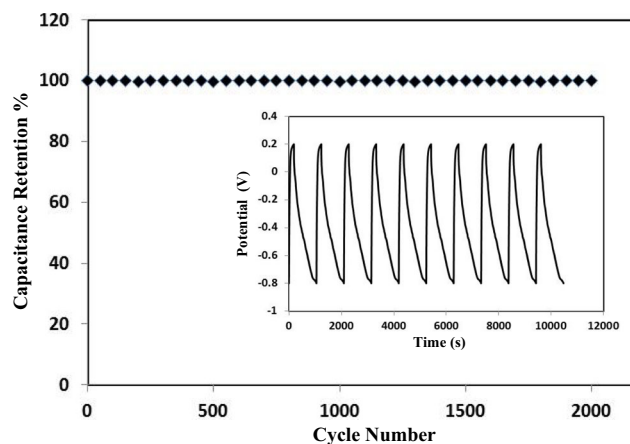


Fig. 9 Cycle stability of ternary G/CoF/PANI nanocomposites during the long-term charge/discharge process at a current density of 1 A g^{-1}

initial capacitance and exhibited prevalent limit reversibility in consecutive charge/discharge cycles. The excellent stability of ternary G/CoF/PANI may be appended to the synergistic impacts among the three components of the ternary system. This may be because the graphene proceeds some mechanical deformation during the redox process of PANI [35], and at the same time, CoFe_2O_4 particles can be stabilized by PANI, which acts as a protective layer, all of these help in enhancing the electrochemical stability.

In order to demonstrate the electrical resistance and the capacitance behavior of the electrodes, impedance measurements were done. The results are given in Fig. 10. The half circle and a straight line of the EIS at the relating high- and low-frequency regions point to the charge transfer resistance and electrical double-layer capacitor (EDLC) of the electrodes (based on ion adsorption), respectively [36]. As shown in Fig. 10, the half circles of the electrode material decreased with introducing graphene into the electrode composition, indicating the decrease of charge transfer resistances of the electrodes. Meanwhile, the straight lines become more vertical for a binary system, representing the higher EDLC behavior. The charge transfer resistance in the ternary system is lower than that in the binary one, emphasizing the faster rate of charge transfer in the ternary system. The magnitude of equivalent series resistance (ESR) is obtained from x-intercept of the Nyquist plot. It has the values of 1.91, 2.05, 1.83, 1.65, 1.46, and $1.32 \text{ } \Omega$ for G/CoF, CoF/PANI, G/PANI, G/NiF/PANI, G/Mag/PANI, and G/CoF/PANI electrodes, respectively. The difference in ESR of electrodes can be attributed to the diverse conductivities of electrode materials. The smaller ESR of ternary electrodes exhibited the lowest charge transfer resistance between the electrolyte and the ternary electrodes due to the synergetic effect of the three components.

From the frequency (f° , Hz) corresponding to the maximum of imaginary impedance (Z'') of the semicircle in the impedance spectra, the time constant (τ , s) of the capacitor is calculated using the following equation: $\tau = 1/f^\circ$

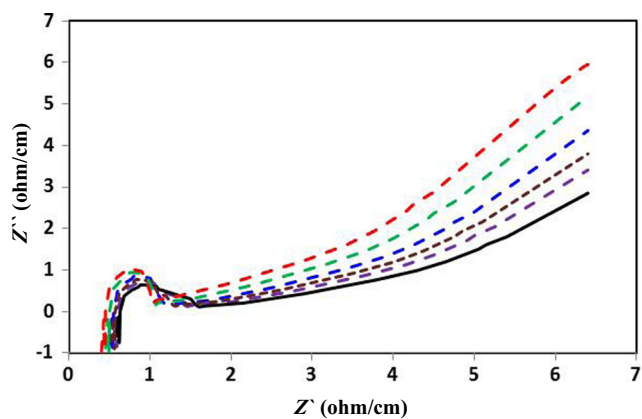


Fig. 10 Impedance spectra of G/CoF (red dashed line), CoF/PANI (green dashed line), G/PANI (royal blue dashed line), G/NiF/PANI (brown dashed line), G/Mag/PANI (violet dashed line), and G/CoF/PANI (black continuous line)

[37, 38]. The values of τ obtained from the data are 4.7, 5.2, 7.1, 12.2, 12.6, 14.1, 14.8, 15.2, 18, 18.1, 35, 48, and 61 ms for G/CoF/PANI, G/NiF/PANI, G/PANI, G/Mag/PANI, G, G/CoF, PANI/CoF, PANI/NiF, PANI/Mag, G/Mag, CoF, NiF, and Mag, respectively. The difference in the time constant is due to structural changes in the electrodes of the electrochemical capacitors. Low values of τ are preferred for electrochemical capacitors for fast charge–discharge processes [39]. The small time constants of the ternary system reveal their high power response.

In order to determine the electrochemical performance of the ternary system electrodes (have higher C_{sp}), the power (P , Wkg^{-1}) and the energy density (E , Wh kg^{-1}) were evaluated using the following equations [40]:

$$E = 0.5 C_{sp} (\Delta V)^2 \quad (3)$$

$$P = E/t \quad (4)$$

where C_{sp} is the specific capacitance of the supercapacitor (Fg^{-1}), ΔV is the voltage change during the discharge process after IR drop in V and t (h) is the time for a sweep segment. The results obtained are illustrated in Fig. 11 as Ragone plots (E vs. P). The energy density was found to decrease gradually with power density. The energy density of G/CoF/PANI is 240 Wh kg^{-1} at a power density of 2680 Wkg^{-1} and at a charging current density of 1 A g^{-1} .

Conclusions

In summary, nanoferrites (Fe_3O_4 , NiFe_2O_4 , CoFe_2O_4), graphene, and PANI hybrid nanomaterials have been prepared. The as-synthesized materials were well characterized

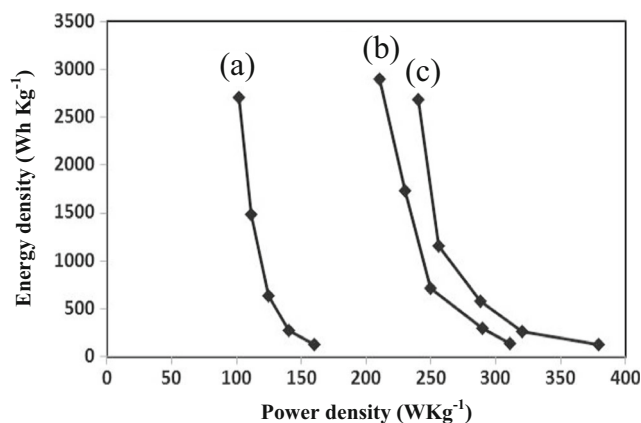


Fig. 11 Ragone plots of (a) G/Mag/PANI, (b) G/NiF/PANI, and (c) G/CoF/PANI calculated from galvanostatic charge/discharge curves (three-electrode system) at different current densities

including the structural and electrochemical properties. The XRD analysis confirmed the formation of a single-phase spinel ferrite. TEM micrographs showed fiber structure for PANI that enables transfer of electrolyte ions. It is found that the well-designed hierarchical nanostructure and the synergistic effects among the three components are assisted for the high electrochemical performance. The as-prepared ternary G/CoF/PANI electrode has much higher specific capacitance, significantly outperforming the three separated components (CoFe_2O_4 , graphene, and PANI) and their corresponding binary hybrids (G/CoF, G/PANI, and CoF/PANI). The ternary hybrid CoF/G/PANI electrode exhibits a specific capacitance reaching 1123 Fg^{-1} , an energy density of 240 Wh kg^{-1} , and a power density of 2680 Wkg^{-1} at a charging current density of 1 A g^{-1} , respectively, and outstanding cycling performance, with 98.2% capacitance retained over 2000 cycles. We trust that this work can open up new conceivable outcomes for investigating novel hybrid electrode materials and their useful application in energy.

References

- Ganesh V, Pitchumani S, Lakshminarayanan V (2006) New symmetric and asymmetric supercapacitors based on high surface area porous nickel and activated carbon. *J Power Source* 158:1523–1532
- Chen J, Jia C, Wan Z (2014) Novel hybrid nanocomposite based on poly(3,4- ethylene dioxythiophene)/multiwalled carbon nanotubes/graphene as electrode material for supercapacitor. *Synth Met* 189: 69–76
- Puscas AM, Carp M, Borza P, Székely I (2009) Measurement considerations on some parameters of supercapacitors. *Acta Univ Sapientiae, J Elect Mech Eng* 1:65–75
- Kurzweil P, Chwistek M, Gallay R (2006) 2nd European Symposium on Supercapacitors & Applications (ESSCAP), Lausanne, 2–3 November 2006

5. Wang H, Hao Q, Yang X, Lu L, Wang X (2009) Graphene oxide doped polyaniline for supercapacitors. *Electrochem. Commun* 11: 1158–1161
6. Gomez-Navarro C, Weitz RT, Bittner AM, Scolai M, News A, Burghard M, Kern K (2007) Electronic transport properties of individual chemically reduced graphene oxide sheets. *Nano Lett* 7: 3499–3503
7. Stoller MD, Park S, Zhu Y, An J, Ruoff RS (2008) Graphene-based ultracapacitors. *Nano Lett* 8:3498–3502
8. Zhang K, Zhang L, Zhao XS, Wu J (2010) Graphene/polyaniline nanofiber composites as supercapacitor electrodes. *Chem Mater* 22: 1392–1401
9. Ye JS, Cui HF, Litu X, Lim TM, Zhang WD, Sheu FS (2005) Preparation and characterization of aligned carbon nanotube-ruthenium oxide nanocomposites for supercapacitors. *Small* 1: 560–565
10. Adekunle AS, Ozoemena KI, Mamba BB, Agboola BO, Oluwatobi OS (2011) Supercapacitive properties of symmetry and the asymmetry two electrode coin type supercapacitor cells made from WCNTS/nickel oxide nanocomposite. *Int J Electrochem Sci* 6: 4760–4774
11. Lee YH, An KH, Lee JY, Lim SC (2007) Carbon nanotube-based supercapacitor in: H.S. Nalwa (ed) *Encycl. Nanosc. Nanotechnol* 1: 625–634
12. Adekunle AS, Ozoemena KI (2008) Electron transfer behaviour of single-walled carbon nanotubes electro-decorated with nickel and nickel oxide layers. *Electrochim Acta* 53:5774–5782
13. Adekunle AS, Ozoemena KI (2008) Insights into the electro-oxidation of hydrazine at single-walled carbon-nanotube-modified edge-plane pyrolytic graphite electrodes electro-decorated with metal and metal oxide films. *J Solid State Electrochem* 12:1325–1336
14. Novoselvo KS, Geim AK, Morozov SV, Jiang D, Katsnelson MI, Grigorieva IV, Dubonos SV, Firsov AA (2005) Two-dimensional gas of massless Dirac fermions in grapheme. *Nature* 438:197–200
15. Jannik CM, Geim AK, Katsnelson MI, Ovoselov MI, Booth TJ, Roth S (2007) The structure of suspended graphene sheets. *Nature* 446:60–63
16. Nderade AL, Valente MA, Ferreira JMF, Fabris JD (2012) Preparation of size-controlled nanoparticles of magnetite. *J Magn Magn Mater* 324:1753–1757
17. Luźny W, Śniechowski M, Laska J (2002) Structural properties of emeraldine base and the role of water contents: X-ray diffraction and computer modelling study. *Synth Met* 126:27–35
18. Klug HP, Alexander LE (1970) X-ray diffraction procedures for polycrystalline and amorphous materials. Wiley, New York
19. Xie K, Qin X, Wang X, Wang Y, Tao H, Wu Q, Yang L, Hu Z (2012) Carbon nanocages as supercapacitor electrode materials. *Adv Mater* 24:347–352
20. Tan Q, Xu Y, Yang J, Qiu L, Chen Y, Chen X (2013) Preparation and electrochemical properties of the ternary nanocomposite of polyaniline/activated carbon/TiO₂ nanowires for supercapacitors. *Electrochim Acta* 88:526–529
21. Gomes EC, Oliveira MAS (2012) Chemical polymerization of aniline in hydrochloric acid (HCl) and formic acid (HCOOH) media. Differences between the two synthesized polyanilines. *Am J Polym Sci* 2:5–13
22. Farrokhzad H, Gerven TV, Bruggen BVD (2013) Preparation and characterization of a conductive polyaniline/polysulfone film and evaluation of the effect of co-solvent. *Eur Polym J* 49:3234–3243
23. Waldron RD (1955) Infrared spectra of ferrites. *Phys Rev* 99:1727
24. Jacob BP, Kumar A, Pant RP, Singh S, Mohammed EM (2011) Influence of preparation method on structural and magnetic properties of nickel ferrite nanoparticles. *Bull Mater Sci* 34:1345–1350
25. Gui Y, Yuan J, Wang W, Zhao J, Tian J, Xie B (2014) Facile solvothermal synthesis and gas sensitivity of graphene/WO₃ nanocomposites. *Materials* 7(6):4587–4600
26. Yan J, Wei T, Fan Z, Qian W, Zhang M, Shen X, Wei F (2010) Preparation of graphene nanosheet/carbon nanotube/polyaniline composite as electrode material for supercapacitors. *J Power Sources* 195:3041–3045
27. Han D, Xu P, Jing X, Wang J, Yang P, Shen Q, Liu J, Song D, Gao Z, Zhang M (2013) Trisodium citrate assisted synthesis of hierarchical NiO nanospheres with improved supercapacitor performance. *J Power Sources* 235:45–53
28. Frackowiak E, Beguin F (2002) Electrochemical storage of energy in carbon nanotubes and nanostructured carbons. *Carbon* 40:1775–1787
29. Qi T, Jiang J, Chen H, Wan H, Miao L, Zhang L (2013) Synergistic effect of Fe₃O₄/reduced graphene oxide nanocomposites for supercapacitors with good cycling life. *Electrochim Acta* 114: 674–680
30. Lim YS, Tan YP, Lim HN, Huang NM, Tan WT, Yarmo MA, Yang YC (2014) Potentiostatically deposited polypyrrole/graphene decorated nano-manganese oxide ternary film for supercapacitors. *Ceram Inter* 40:3855–3864
31. Yan D, Li Y, Liu Y, Zhuo R, Geng B, Wu Z, Wang J, Ren P, Yan P (2015) Design and influence of mass ratio on supercapacitive properties of ternary electrode material reduced graphene oxide@MnO₂@ poly(3,4-ethylenedioxythiophene)-poly(styrene sulphonate). *Electrochim Acta* 169:317–335
32. Rajagopalan B, Chung J (2014) Reduced chemically modified graphene oxide for supercapacitor electrode. *Nanoscale Res Lett* 9:535–545
33. Farsi H, Gopal F, Barzgar Z (2013) A study of hydrated nanostructured tungsten trioxide as an electroactive material for pseudocapacitors. *Ionics* 19:287–294
34. Jiang TQJ, Chen H, Wan H, Miao L, Zhang L (2013) Synergetic effect of Fe₃O₄/reduced graphene oxide nanocomposites for supercapacitors with good cycling life. *Electrochim Acta* 114: 674–680
35. Xiong P, Huang H, Wang X (2014) Design and synthesis of ternary cobalt ferrite/graphene/polyaniline hierarchical nanocomposites for high-performance supercapacitors. *J Power Source* 245:937–946
36. Yan L, Hongrui P, Guicun L, Kezheng C (2012) Synthesis and electrochemical performance of sandwich-like polyaniline/graphene composite nanosheets. *Eur Polym J* 48:1406–1412
37. Balasubramaniam M, Balakumar S (2016) Exploration of electrochemical properties of zinc antimonate nanoparticles as supercapacitor electrode material. *Mater Sci Semicond Process* 56:287–294
38. Daniel V (1967) Dielectric relaxation. Academic Press, London and New York
39. Burke A (2000) Ultracapacitors: why, how, and where is the technology. *J Power Sources* 91:17–50
40. Zhu J, Chen M, Qu H, Luo Z, Wu S, Colorado HA, Wei S, Guo Z (2013) Magnetic field induced capacitance enhancement in graphene and magnetic graphene nanocomposites. *Energy Environ Sci* 6:194–204